

---

This is an electronic reprint of the original article.  
This reprint may differ from the original in pagination and typographic detail.

Song, Kezhou; Jokilaakso, Ari

## CFD modeling of the multiphase flow in an SKS furnace—The effect of melt density and viscosity

*Published in:*  
Chemical Engineering Journal Advances

*DOI:*  
[10.1016/j.cej.2023.100496](https://doi.org/10.1016/j.cej.2023.100496)

Published: 15/05/2023

*Document Version*  
Publisher's PDF, also known as Version of record

*Published under the following license:*  
CC BY-NC-ND

*Please cite the original version:*  
Song, K., & Jokilaakso, A. (2023). CFD modeling of the multiphase flow in an SKS furnace—The effect of melt density and viscosity. *Chemical Engineering Journal Advances*, 14, Article 100496.  
<https://doi.org/10.1016/j.cej.2023.100496>

---

This material is protected by copyright and other intellectual property rights, and duplication or sale of all or part of any of the repository collections is not permitted, except that material may be duplicated by you for your research use or educational purposes in electronic or print form. You must obtain permission for any other use. Electronic or print copies may not be offered, whether for sale or otherwise to anyone who is not an authorised user.



## CFD modeling of the multiphase flow in an SKS furnace—The effect of melt density and viscosity

Kezhou Song, Ari Jokilaakso\*

School of Chemical Engineering, Department of Chemical and Metallurgical Engineering, Aalto University, P.O. Box 16100, Kemistintie 1, Espoo 02150, Finland

### ABSTRACT

A previously reported numerical method using the multi-fluid VOF model to simulate an SKS furnace multiphase flow was further verified to provide a good reference for the macroscopic flow field simulation of industrial vessels with similar geometry. Using the verified numerical model, CFD simulation of a full-scale SKS furnace multiphase flow was conducted, targeting the agitation performance with different melt densities and viscosities, under constant furnace operating conditions. According to this simulation, the melt density and viscosity in a common applied range in industry is not able to significantly affect the bath agitation efficiency like other parameters, such as the tuyere diameter and bath depth. More specifically, the results indicate that an increased melt density or viscosity slightly weakens the melt flow motion, and increases the wall shear stress. Since variation in melt density and viscosity is common in industry, the results from this simulation offer a good basis for the estimation of SKS furnace operating performance and the adjustment of the physical properties of the melt in SKS furnaces or other similar industrial vessels.

### 1. Introduction

During the last decade, Computational Fluid Dynamics (CFD) has been applied to improve the operational efficiency of the bottom blown smelting furnace (the ShuiKouShan furnace, or SKS). This is due to the increasing interest and demands placed on this newly emerging metallurgical technology [1,2]. SKS technology was first commercially used in lead making processes and has gradually become more widespread in copper and other metal smelting or converting furnaces [1,2]. With more promising properties explored, growing production capacity for SKS technology has been noticed, which may continue with further optimization [1,2].

Even though the use of SKS technology is increasing in eastern Asia [1], SKS furnaces are still being operated without a thorough understanding of the effect of furnace operating parameters and furnace structures. Some adjustments to the SKS furnace have not originated wholly from modeling research; instead, assumptions have been made based on onsite observations or tests. Therefore, some adjustments do not always result in smooth operation, and once the practical requirements are not met, for instance, when the lining refractories are subjected to strong impact and erode unexpectedly, extra furnace operation costs are incurred. Scientific SKS furnace modeling research is necessary to achieve better operation [3]. To support the industrial demand for better furnace operating performance, CFD modeling studies have been widely conducted and reported [4–9].

Currently, the reported SKS furnace modeling research has been carried out using different numerical methods and model verification approaches. The VOF model has been mostly used in bubbly flow simulation regarding different types of metallurgical bath smelting reactors [10,11], and was first used in SKS furnace simulation by Yan et al. in 2012 [4]. The VOF model was found to be able to describe the general shape of bubbles and plumes; thus it was used to predict basic flow characteristics under different conditions [4,10,11]. In 2019, an SKS furnace modeling research study using a Eulerian model was reported, and the results showed that the simulated mixing time agreed with the corresponding water model experiments [6]. Based on the reported modeling experiences, in our previous research in 2021, the multi-fluid VOF model that coupled VOF and Eulerian models was applied for the simulation of the SKS furnace flow field [7–9]. It was found that the plume shape had been accurately predicted, and the surface waves, which could be an indicator of the basic flow features [12–13], were in good agreement with the reported water model experiments. CFD modeling research on the flow phenomena of SKS furnaces using different numerical models is shown in Table 1.

The progress of the numerical scheme has contributed to further investigation into the factors affecting the SKS furnace flow field. These factors, including gas flow rate, tuyere angles, tuyere diameters, and bath depths, have been the main focus in the past 10 years. Apart from these parameters, a change in temperature and melt components also affects the melt fluidity, thus influencing the furnace operating

\* Corresponding author.

E-mail address: [ari.jokilaakso@aalto.fi](mailto:ari.jokilaakso@aalto.fi) (A. Jokilaakso).

efficiency. However, due to the lack of industrial data and probably feasible numerical schemes, currently no such SKS furnace CFD modeling research has been reported. Therefore, to reveal the corresponding influences, other methods should be considered. One feasible way is to transfer the changes in temperature and melt components to other relative parameters which directly affect fluidity. With a change in temperature, the density and viscosity of slag, matte, or metal would increase or decrease, and similarly, such variation would occur when the melt chemical components are adjusted. For instance, the Fe/Si ratio in copper smelting slag is not constant, due to the reaction progress or other industrial requirements. With a growing Fe/Si ratio, the viscosity of fayalite slag decreases [14,15], therefore becoming more fluid, which increases the bath agitation. As the melt fluidity is directly influenced by changes in the physical properties of the melt, modeling work could be conducted by changing the melt density and viscosity, which are functions of temperature and melt composition [15].

In this simulation, the effect of melt density and viscosity on bath agitation performance was investigated. To expand the application of the results, the simulated density and viscosity range was taken from the data of both copper smelting SKS furnaces and lead making SKS furnaces. Therefore, this simulation should supply reliable information to industry about the relations between agitation efficiency and the physical properties of the melt. Besides, the numerical model in this simulation, which was used in the previous studies, has been further verified, and could be a feasible choice for industrial vessels with similar geometry.

## 2. Mathematical model

The performance of the multi-fluid VOF model adopted in this simulation was verified in our previous CFD study [7]. The description of the mathematics is given below.

### 2.1. Governing equations

The mass and momentum conservation equations for phase  $q$  (including the gas phase and liquid phase) are given as Eqs. (1) and (2) [16], respectively:

$$\frac{\partial}{\partial t}(\alpha_q \rho_q) + \nabla \cdot (\alpha_q \rho_q \vec{v}_q) = 0 \quad (1)$$

$$\frac{\partial}{\partial t}(\alpha_q \rho_q \vec{v}_q) + \nabla \cdot (\alpha_q \rho_q \vec{v}_q \vec{v}_q) = -\nabla p + \nabla \cdot \left[ \mu \left( \nabla \vec{v}_q + \nabla \vec{v}_q^T \right) \right] + \alpha_q \rho_q \vec{g} + \vec{f} \quad (2)$$

$$\alpha_q = \alpha_g \text{ or } \alpha_l, \quad \alpha_g + \alpha_l = 1 \quad (3)$$

In Eqs. (1)-(3),  $\alpha$  is the volume fraction,  $\rho$  is the density,  $\vec{v}$  is the velocity,  $p$  is the pressure shared by both two phases,  $\alpha_q \rho_q \vec{g}$  is the

gravity term, and  $\vec{f}$  is an external body force which is specifically defined as the drag force in the current system. The subscripts  $g$  and  $l$  represent the gas and liquid phases, respectively.

### 2.2. Drag force

In the current simulation, due to a very high injection speed, the drag force is preferentially considered, ignoring other interphase forces, such as the turbulence dispersion force, which usually influence the flow field in a much lower speed range. Since detailed bubble behavior is not discussed in this work, the simplification does not affect the result analysis and helps to improve the calculation efficiency. Drag force is introduced based on the symmetric model provided by the multi-fluid VOF model [16]. For the symmetric model, density and viscosity are calculated from volume averaged properties:

$$\rho_{gl} = \alpha_g \rho_g + \alpha_l \rho_l \quad (4)$$

$$\mu_{gl} = \alpha_g \mu_g + \alpha_l \mu_l \quad (5)$$

and the diameter of bubbles or droplets is defined as

$$d_{gl} = \frac{1}{2}(d_g + d_l) \quad (6)$$

In turn, the drag function is given as

$$f = \frac{C_D Re}{24} \quad (7)$$

where the relative Reynold number  $Re$  is

$$Re = \frac{\rho_{gl} |\vec{v}_g - \vec{v}_l| d_{gl}}{\mu_{gl}} \quad (8)$$

and the drag coefficient  $C_D$  is

$$C_D = \begin{cases} 24(1 + 0.15Re^{0.687})/Re & Re \leq 1000 \\ 0.44 & Re \geq 1000 \end{cases} \quad (9)$$

The drag force is only affected by the bubble or droplet diameter, since the values of the other variables are all taken from industrial data. In the SKS furnace, the gas injection speed for the quasi-jetting flow regime is very high, compared to the common situation in other bath smelting processes with bubbly flow regimes [10,11,17]. The bubbles aggregate into a bubble group or bigger bubbles of irregular shape, according to the experimental photographs from Shui et al. [12]. Therefore, as the bubbles tend to aggregate and probably coalesce, consideration is given primarily to the continuity of the bubble plume. As proposed earlier [7], the bubble plume is regarded as a bubble ribbon. This enables the gas phase to be set as a continuous phase and hence the droplet diameter is defined instead. The diameter value was

**Table 1**  
Reported CFD simulations on the flow phenomena in an SKS furnace.

Research group	Model	Model scale	Model verification	Liquid phase	Tuyere diameter	Research output	Ref.
Yan et al. 2012	VOF	Single tuyere (2D)	Bubble shape	Matte	60 mm	Optimization of tuyere angle and diameter	[4]
Dong et al. 2019	VOF	Full-scale (3D)	Plume shape	Slag-matte	Unreported	General analysis of flow field and splashing	[5]
Shao et al. 2019	Eulerian	Scaled- down (3D)	Mixing time	Matte	Unreported	Optimization of tuyere arrangements and gas flow rate	[6]
Song and Jokilaakso 2021	Multi-Fluid VOF	Scaled- down (3D)	Plume shape and wave characteristics	Matte	60 mm	Effect of tuyere arrangements	[7]
Song and Jokilaakso 2021	Multi-Fluid VOF	Scaled- down (3D)	Plume shape and wave characteristics	Matte	48 mm, 60 mm	New tuyere arrangements	[8]
Song and Jokilaakso 2021	Multi-Fluid VOF	Scaled- down (3D)	Plume shape and wave characteristics	Matte	48 mm, 60 mm	Effect of tuyere diameter and bath depth	[9]

determined based on whether the plume shape (or ribbon shape) agreed with the experimental images [12], and finally the default value of 0.00001 m was adopted.

### 2.3. Turbulence models

The standard  $k$ - $\varepsilon$  turbulence model with standard wall functions was adopted for the present simulation. The kinetic energy  $k$  and its rate of dissipation  $\varepsilon$  yields are as follows:

$$\frac{\partial}{\partial t}(\rho_m k) + \nabla \cdot (\rho_m \vec{v}_m k) = \nabla \cdot \left( \alpha \frac{\mu_t}{\sigma_k} \nabla k \right) + G_k + G_b - \rho_m \varepsilon \quad (10)$$

$$\frac{\partial}{\partial t}(\rho_m \varepsilon) + \nabla \cdot (\rho_m \vec{v}_m \varepsilon) = \nabla \cdot \left( \frac{\mu_t}{\sigma_\varepsilon} \nabla \varepsilon \right) + \frac{\varepsilon}{k} (C_{1\varepsilon}(G_k + G_b)) - \frac{\varepsilon^2}{k} C_{2\varepsilon} \rho_m \quad (11)$$

where  $G_k$  represents the generation of turbulence energy due to the mean velocity gradients, and  $G_b$  is the turbulence energy due to buoyancy. The mixture density  $\rho_m$  and mixture velocity  $\vec{v}_m$  are defined as follows:

$$\rho_m = \alpha_g \rho_g + \alpha_l \rho_l \quad (12)$$

$$\vec{v}_m = \frac{\alpha_g \rho_g \vec{v}_g + \alpha_l \rho_l \vec{v}_l}{\alpha_g \rho_g + \alpha_l \rho_l} \quad (13)$$

The empirical constants are  $C_{1\varepsilon} = 1.44$ ,  $C_{2\varepsilon} = 1.92$ ,  $\sigma_k = 1$ , and  $\sigma_\varepsilon = 1.3$ . The turbulence viscosity  $\mu_t$  is given as Eq. (14):

$$\mu_t = \rho_m C_\mu \frac{k^2}{\varepsilon}, \quad C_\mu = 0.09 \quad (14)$$

## 3. Geometry and simulation conditions

### 3.1. Physical model

In this work, a simulated SKS furnace model was created for a prototype at a ratio of 1:1. The related parameters are shown in Table 2. The tuyere angle combination was  $0^\circ$  &  $16^\circ$  as shown in the Fig. 1. The tuyere diameter is 48 mm, which are optimized tuyere arrangements according to our previous research [8,9]. The density and viscosity

**Table 2**

Parameters of the prototype, water model, simulated water model, and the simulated SKS furnace.

	Prototype [18,20,21]	Water model	Simulated water model	Simulated SKS furnace
Inner diameter [mm]	3490	290	290	3480
Length [mm]	15,084	1250	1250	15,000
Number of operational tuyeres	9	5	5	9
Tuyere diameter [mm]	60	4	4	48
Tuyere angle	$7^\circ + 22^\circ$	$16^\circ$	$16^\circ$	$0^\circ + 16^\circ$
Depth of liquid [mm]	1200 - 1800	120	120	1715
Gas volumetric flow rate [ $\text{m}^3 \cdot \text{h}^{-1}$ ]	5000 - 15,000 (in total)	8.4	8.4	12,000 (in total)
Gas/Gas density [ $\text{kg} \cdot \text{m}^{-3}$ ]	Enriched oxygen/1.38	Air/-	Air/1.225	Enriched oxygen/1.38
Liquid density [ $\text{kg} \cdot \text{m}^{-3}$ ]	4440	-	1000	3000-5000
Liquid viscosity [Pa·s]	0.004	-	0.001	0.002-2.000
Liquid interface tension [ $\text{N} \cdot \text{m}^{-3}$ ]	0.33	-	0.071	0.33

values are taken from published industrial data [18] and onsite measurements at Henan Yuguang Gold Lead Company Limited [19]. The density was in the range of 3000–5000  $\text{kg} \cdot \text{m}^{-3}$ , according to the properties of matte and slag in copper smelting furnaces and lead oxidation/reduction furnaces. The viscosity was in the range of 0.002–2.000 Pa·s, a common variation range for the slag phase, which is the main phase by volume in lead oxidation/reduction furnaces. For all the presented cases, the total volumetric gas flow rate was 12,000  $\text{m}^3 \cdot \text{h}^{-1}$ , which is in the range of the commonly operated 5000–15,000  $\text{m}^3 \cdot \text{h}^{-1}$  for SKS copper smelting.

To improve the calculation efficiency, the following simplifications were implemented in the physical model:

- 1) The furnace structure was simplified as a simple cylinder.
- 2) There is no heat and mass transfer in the physical model. The temperature changes due to heat losses or heat transfer were considered to be so low that their impact on melt viscosity or density was negligible.
- 3) There is no second liquid phase present in the model, to avoid unnecessary interference. This study focuses on the agitation performance under conditions of different liquid physical parameters, rather than on the interaction between matte/metal and slag layers.

### 3.2. CFD model and verification

The CFD setup is the same as in the previous studies due to its good performance in calculation efficiency and result reliability [7–9]. The mesh of the simulated SKS furnace is shown in Fig. 2. Hexahedral mesh was constructed with multizone meshing. Using the same mesh treatment as that of our previous work, the gas inlets of very small size (diameter 48 mm, less than 1/70 of the furnace section diameter) were simplified and made square to improve the mesh quality and calculation efficiency. The simplification was verified by a mesh test to make sure that the macroscopic velocity distribution and wall shear stress were not affected by the inlet mesh treatment and mesh size [7]. The number of cells with the current meshing setup was eventually set at around 300 000, with more than 99.80% of the elements of a skewness below 0.50, which translates into good or excellent cell quality, and the others, less than 0.20%, of a skewness below 0.58, evaluated as fair cell quality [22].

As shown in Fig. 2, the gas inlets are located at the furnace bottom (the grid goes through the cylinder and is visible on both surfaces) and set as the velocity inlet. The gas outlet is located at the top surface at a distance from the agitation zone and was set as the pressure outlet. The time-step was set as  $5 \times 10^{-4}$  s, and the convergence marked by a dimensionless residual of less than  $1 \times 10^{-3}$ . All of the control equations in this simulation were calculated using the commercial software Ansys Fluent.

In our previous study, the numerical model was proved to be capable of geometrically reconstructing the bubble plumes in terms of plume position and plume shape. Furthermore, the wave characteristics were found to agree well with the experimental water model tests reported by Shui et al. [12]. The dimensionless wave frequency of the simulated water model was found to be 1.495, which is very close to the reported 1.566 of the corresponding water model experiment [12]. The wave

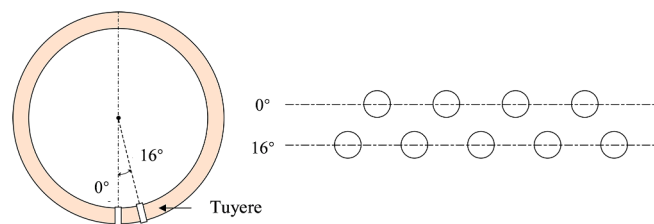


**Fig. 1.** Schematic diagram of the tuyere angle and tuyere arrangements for this simulation.

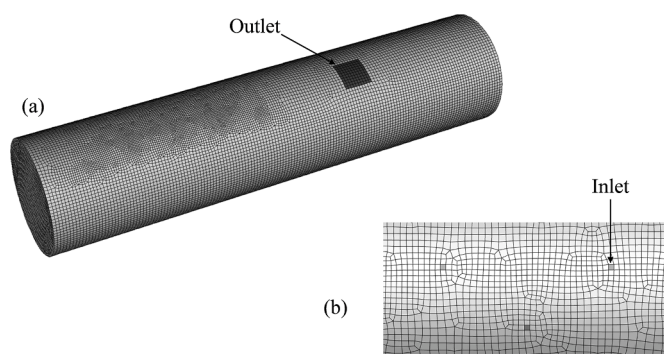


Fig. 2. (a) Mesh of the simulated SKS furnace. (b) Mesh arrangement of the tuyere area. Cells in dark gray are the inlets where tuyeres are located.

amplitude was also in the reported range derived from the water model test results gained in very similar conditions [7]. In the previous verification, the simulated water model was a single-nozzle slice model, which could be regarded as part of the multi-nozzle water model reported in the literature. The simulated slice model leads to a stronger interaction between the wave and wall. Therefore, the simulated wave amplitude was in an increasing trend and would further increase beyond the amplitude range reported in the literature.

To avoid any unexpected model error overlooked in the previous verification, a new experiment was conducted in a similar way with a scaled-down water model and a simulated one with the same nozzle arrangements and model size. The detailed model parameters can be seen in Table 2. In this new verification experiment, the result presented the same wave frequency and an almost identical wave amplitude, and was recorded as a short numerical model verification video. The video is provided as supplementary data attached to the Appendix. A screenshot from the video is shown as Fig. 3, in which asymmetric standing waves appear at the same time and can be compared directly. The wave comparison between the water model and the simulated water model from the whole video is presented in Fig. 4, which shows that the simulated waves are generated periodically and the wave amplitudes are all in the range measured from the water model. A more visualized comparison can be seen in the video, showing that wave characteristics of both models displayed were in good agreement. As the standing waves could only be generated at a certain gas injection speed and bath depth, the model verification experiments indicated that, under the same or similar conditions, an extremely similar flow field could be constructed using the current numerical model. The other related detailed verification processes and figures can be seen in our previous work [7].

#### 4. Results and discussion

In this study, the effect of the melt density and viscosity on the SKS

flow field is presented and analyzed. By comparing the simulation results under different conditions, variations in the macroscopic flow fields were found. The variables investigated for this simulation are listed in Table 3. The density was set within the range of 3000–5000 kg/m<sup>3</sup>, which is a common range for the matte and slag density in the copper smelting processes, and for slag density in lead oxidation and reduction processes. The viscosity was in the range of 0.002–0.2 Pa·s, from which the lower range was mostly for the melted matte or metal, and the upper range for the slag. To widen the adaptability of the results, other parameters including pool depth and gas injection speed were selected in a comparatively higher range, as an intensified flow field is expected in industry. The surface tension which would influence the low velocity region is taken from the reported industrial data (shown in Table 2), to be close to most of the industrial situations.

The simulation results were derived from a certain period within the simulation time range of 0–30 s. To visualize the results, an agitation zone was selected (shown in Fig. 5) in which the low velocity region was exhibited (see Sections 4.1, 4.2), and the corresponding region volume fraction was also calculated.

In an SKS furnace, the bath melt is fiercely agitated by the high-speed gas that is injected. In the zones surrounding a plume which are of higher matte velocity, the physical interaction between the high temperature liquid and gas is strong, and the chemical reactions will progress efficiently. However, for the low velocity regions located at the far side of the plume, where the injected gas barely reaches, the reaction efficiency could depend on circular melt flow. To enhance the gas-liquid contact in the whole bath, it is necessary to reduce the volume of the low velocity regions. Hence, in this simulation, the distribution of low velocity regions is regarded as a crucial point in evaluating the general agitation performance. A low velocity region is defined as an area with a matte velocity of below 0.3 m·s<sup>-1</sup>. To be in this velocity range, the corresponding low velocity regions are mostly distributed in the area near the wall, and are clearly displayed in the figures below.

##### 4.1. The effect of melt density

The common range for copper matte density is 3000–5000 kg/m<sup>3</sup>. This range also covers the range of slag density, which is mostly in a lower range below 4000 kg/m<sup>3</sup> for the copper and lead making processes. Therefore, in this section, the simulated melt could be regarded as a matte or slag phase in industry, with corresponding densities.

The distribution of low velocity regions with a different melt density, corresponding to Cases 1–3 in Table 3, is shown in Fig. 6. Images of the low velocity regions were recorded every 0.5 s during a period of 20–30 s. To show the situation at each of these moments, a total of 21 images for each moment were overlapped with 95% transparency. These overlapped images are shown in Figs. 6(a)–(c), corresponding to cases in the conditions of a melt density of 3000 kg/m<sup>3</sup>, 4000 kg/m<sup>3</sup>, and 5000 kg/m<sup>3</sup>, respectively. The detailed low velocity region distribution is illustrated by a gradual color change from red to blue, corresponding to



Fig. 3. A screenshot from the numerical model verification video. The water model is shown on the left and the simulated water model on the right. Conditions: air volumetric speed: 140 L/min, operational nozzle number: 5.

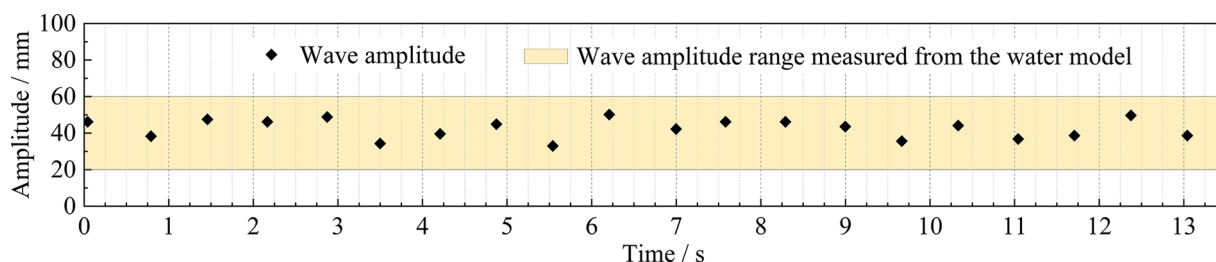


Fig. 4. Evaluation of the standing wave frequency and amplitude in the numerical model verification video. Conditions: air volumetric speed: 140 L/min, operational nozzle number: 5.

Table 3  
Variables investigated.

	Density (kg/m <sup>3</sup> )	Viscosity (Pa·s)	Pool depth (mm)	Tuyere diameter (mm)	Gas injection speed (m/s)
Case 1	3000	0.2	1440	48	198.67
Case 2	4000	0.2	1440	48	198.67
Case 3	5000	0.2	1440	48	198.67
Case 4	4000	0.002	1440	48	198.67
Case 5 (Case2)	4000	0.2	1440	48	198.67
Case 6	4000	2	1440	48	198.67

the velocity from high to low; the frequency of the appearance of a low velocity region can be evaluated by the color saturation.

According to Fig. 6, the low velocity region distributions are basically at the same level for different melt densities, in contrast to the huge difference found with different tuyere diameters or bath depths that have a greater effect on bath agitation, based on the results from the previous research [9]. This indicates that, in the current density range, a change in density is not as important a factor as the previously investigated parameters that strongly affect gas agitation efficiency in their common ranges, such as bath depth and tuyere diameter. In Fig. 6, a slight difference could be found between images (a)-(c), in that the colored regions are of lower saturation in image (a), whereas in images (b)-(c), the low velocity regions are more intensively colored with higher saturation. The saturation gap shows that the agitation zone is comparatively more active in conditions of lower melt density. A quantified low velocity region volume fraction for different melt density is displayed in Fig. 6(d), showing that in the simulated 0–30 s, the volume fractions of the low velocity regions for a density of 4000 kg/m<sup>3</sup> and 5000 kg/m<sup>3</sup> are interlaced, and the volume fraction for a density of 3000 kg/m<sup>3</sup> is mostly below that of the density 5000 kg/m<sup>3</sup>.

In order to reveal the detailed flow phenomena leading to differences in agitation performance under conditions of different matte densities, an air velocity vector distribution was used for analysis, shown in Fig. 7. Figs. 7(a) and (b) are the distributions of air velocity vectors derived from a peak time in the volume fraction curve in Fig. 6(d) for the melt density of 3000 kg/m<sup>3</sup> and 5000 kg/m<sup>3</sup>, respectively. As can be seen, with a melt density of 3000 kg/m<sup>3</sup>, a large circulation area was detected

at the far side of the high-speed bubble plume, due to an enhanced horizontal flow. The circulation accelerates the back flows in the near wall area and reduces the volume of the low velocity regions. In the case of 5000 kg/m<sup>3</sup>, the circulation forms in a smaller area and the flow in the near wall region is at low speed but without a strong back flow. Therefore, the more active flow field could be attributed to a larger circulation area and stronger back flow, as these flow phenomena tend to appear when the drag force is smaller due to a lower melt density.

The wall shear stress is important for the evaluation of the impact on the refractory lining. According to previous studies [9], the wall shear stress correlates to some extent with the velocity distribution. Stronger wall shear stress is mostly located in the area with intensified agitation. However, when the melt density varies, for instance, with a temperature change, the variation in the wall shear stress should not be estimated based simply on experience, because the larger density results in stronger drag force and weakens the agitation, as discussed in relation to Fig. 7. The bottom view of the superimposition of the wall shear stress in conditions of different densities is presented in Fig. 8. In general, there are no significant differences between the different cases. Based on a comparison between Figs. 8(a)-(c), the wall shear stress slightly increases with higher melt density. This suggests that, although higher melt density suppresses the flow motion, the wall shear stress still tends to increase.

#### 4.2. The effect of melt viscosity

According to onsite measurements, the matte and slag viscosity changes in some ranges according to the external environment and internal chemical structures. Sometimes the viscosity variation can be huge and is able to affect the agitation efficiency. In this simulation, the effect of melt viscosity was investigated in order to explore the relations between bath agitation performance and change in melt viscosity. Generally, the slag viscosity for both copper and lead making processes is in the range of 0.002–2.000 Pa·s. This range also covers the range of matte viscosity, which is mostly in a lower range below 0.5 Pa·s. Therefore, in this section, the simulated melt could be regarded as a matte or slag phase with corresponding viscosities.

The distribution of low velocity regions with different slag viscosities, corresponding to Cases 4–6 in Table 3, is shown in Fig. 9. As can be seen from Figs. 9(a)-(c), in the current tested viscosity range, similarly to

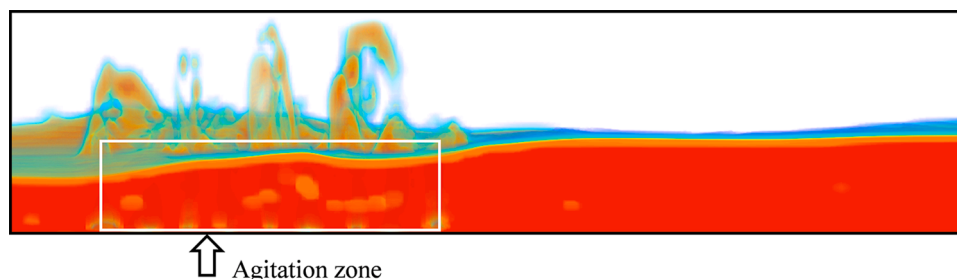
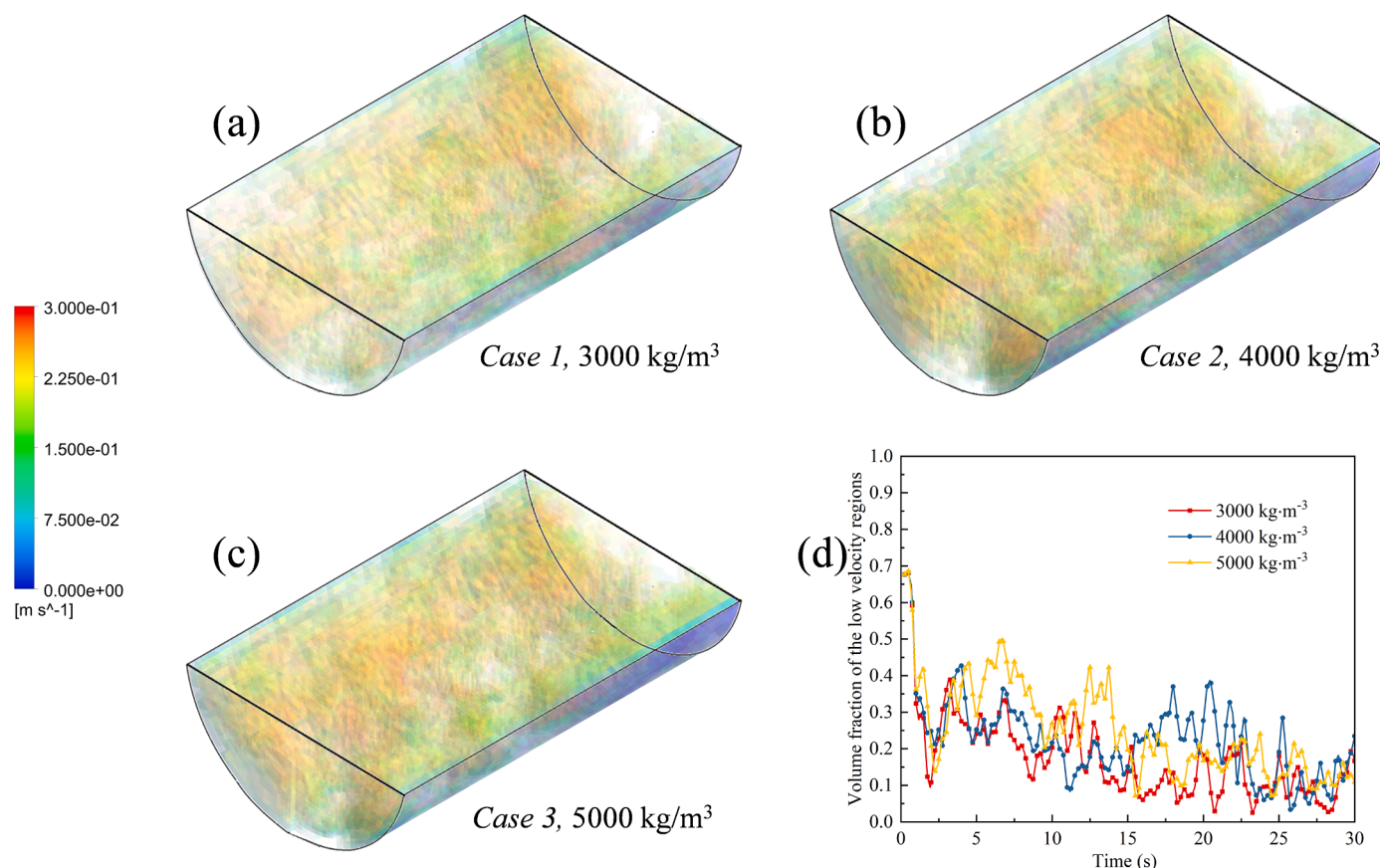
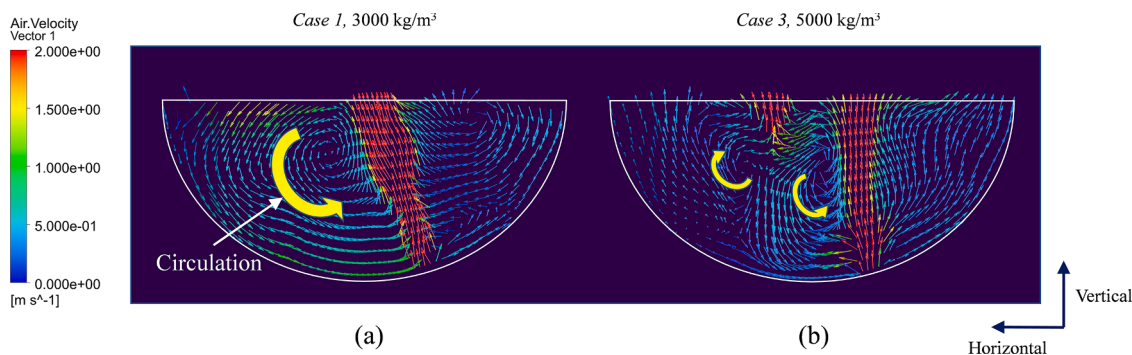


Fig. 5. Agitation zone studied in this simulation.



**Fig. 6.** Distribution of low velocity regions (melt velocity less than  $0.3 \text{ m}\cdot\text{s}^{-1}$ ) with different melt density. Images (a)–(c) are superimpositions of the low velocity regions from 20 to 30 s. The images were taken each 0.5 s, and each image was set with 95% transparency. Conditions: viscosity:  $0.2 \text{ Pa}\cdot\text{s}$ , density: (a)  $3000 \text{ kg}/\text{m}^3$ , (b)  $4000 \text{ kg}/\text{m}^3$ , (c)  $5000 \text{ kg}/\text{m}^3$ . The legend bar on the left shows the velocity estimation for images (a)–(c). Image (d) is the variation in volume fractions of the low velocity regions from 0 to 30 s, with a matte density of  $3000 \text{ kg}/\text{m}^3$ ,  $4000 \text{ kg}/\text{m}^3$ ,  $5000 \text{ kg}/\text{m}^3$ , and a viscosity of  $0.2 \text{ Pa}\cdot\text{s}$ .



**Fig. 7.** Air velocity vectors in the central bubble plume sections for Case 1 (a) density  $3000 \text{ kg}/\text{m}^3$ , time  $25.00 \text{ s}$  and Case 3 (b)  $5000 \text{ kg}/\text{m}^3$ , time  $26.00 \text{ s}$ . The time is selected at a peak in the volume fraction variation curve (Fig. 4(d)) of the low velocity regions.

the effect of melt density, the volume of the colored low velocity regions does not vary a lot with the increase in melt viscosity. This indicates that when the melt viscosity changes in the common range, the agitation performance is slightly affected, but it is not as obvious as the impact of parameters such as bath depth or tuyere diameter. With the increase in melt viscosity, the colored low velocity regions gradually expand and the color saturation also intensifies, which could indicate the more frequent appearances of low velocity regions. Therefore, the agitation zone tends to be quieter when the melt is of higher viscosity. Fig. 9(d) shows the quantified low velocity region volume fractions of Figs. 9(a)–(c) with a wider time range. Before 20 s, the volume fraction curves interlace with each other, and after 20 s, a decreasing trend can be seen

for the viscosity  $0.002 \text{ Pa}\cdot\text{s}$  and  $0.200 \text{ Pa}\cdot\text{s}$ , whereas the curve of  $2.000 \text{ Pa}\cdot\text{s}$  remains steady at a higher level. Such variation basically agrees with the color distribution in Figs. 9(a)–(c); therefore, it can be concluded that higher melt viscosity, which is equivalent to poorer melt fluidity, impairs agitation performance in the investigated conditions.

The melt velocity vectors for the cases of  $0.002 \text{ Pa}\cdot\text{s}$  (Case 4) and  $2.000 \text{ Pa}\cdot\text{s}$  (Case 6) viscosity are shown in Fig. 10. In the case of  $0.002 \text{ Pa}\cdot\text{s}$  viscosity shown in Fig. 10(a), the horizontal flow is at a comparatively higher speed, and a stronger back flow can be seen in the near wall region. When the viscosity is increased, as shown in Fig. 10(b), the horizontal flow seems to encounter stronger resistance and is weakened significantly. Such different agitation performances reflect the

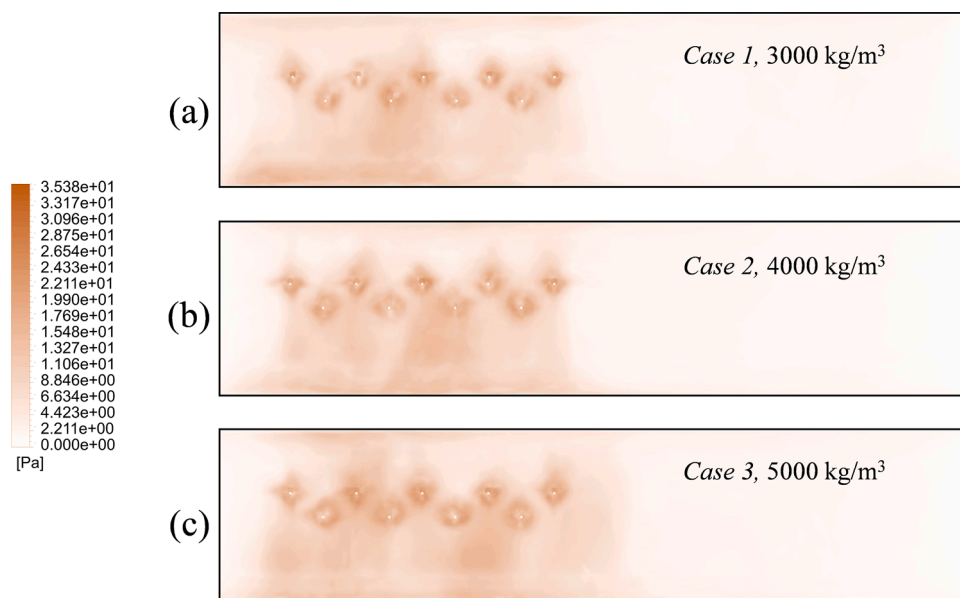


**Fig. 8.** Bottom view of the superimposition of wall shear stress at 20–30 s. The images were taken from each 0.5 s, and each image was set with 95% transparency. Conditions: viscosity: 0.2 Pa·s, density: (a) 3000 kg/m<sup>3</sup>, (b) 4000 kg/m<sup>3</sup>, (c) 5000 kg/m<sup>3</sup>.

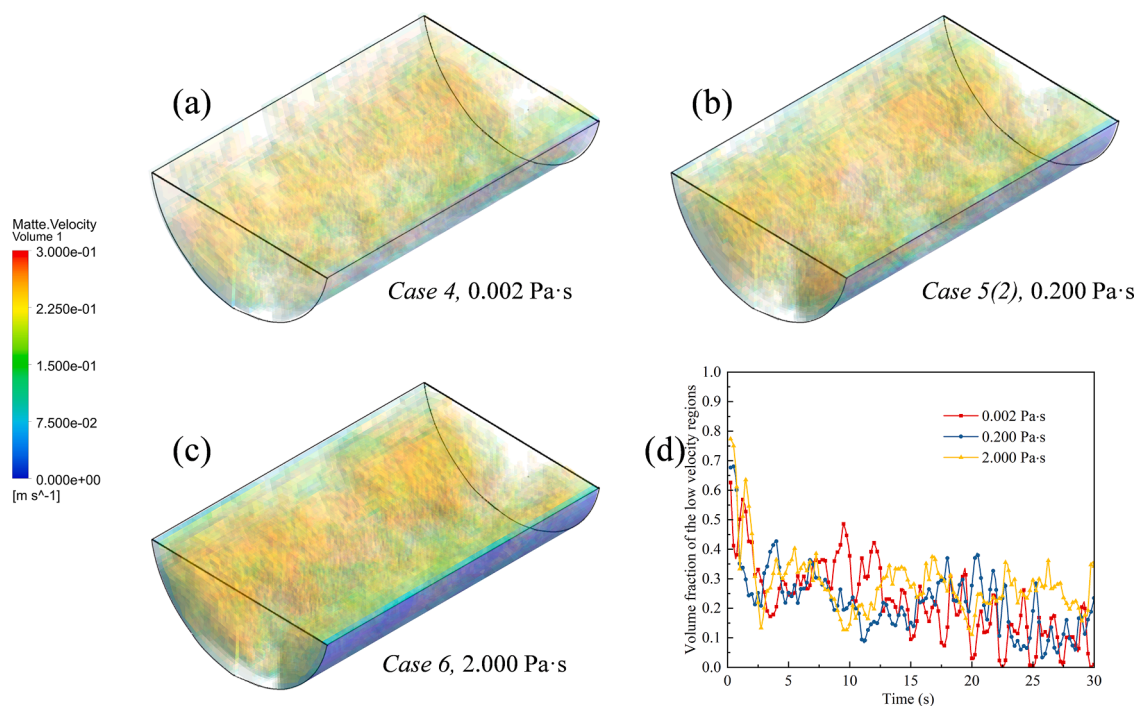


**Fig. 9.** Distribution of low velocity regions (matte velocity less than 0.3 m·s<sup>-1</sup>) with different tuyere diameters. Images (a)–(c) are superimpositions of the low velocity regions from 20 to 30 s. The images were taken from each 0.5 s, and each image was set with 95% transparency. Conditions: density: 4000 kg/m<sup>3</sup>, density: (a) 0.002 Pa·s, (b) 0.200 Pa·s, (c) 2.000 Pa·s. The legend bar on the left shows the velocity estimation for images (a)–(c). Image (d) is the variation in volume fractions of the low velocity regions from 0 to 30 s, with a liquid viscosity of 0.002 Pa·s, 0.200 Pa·s, 2.000 Pa·s, and density of 4000 kg/m<sup>3</sup>.

difference in melt fluidity with different melt viscosities.

The bottom view of the superimposition of the wall shear stress in the different viscosity conditions is presented in Fig. 11. Based on a comparison between Figs. 11(a)–(c), the viscosity in the current investigated range seems to have a strong influence on the wall shear stress distribution, and a significant increase in wall shear stress could be found with a larger melt viscosity. Therefore, in a common situation when the matte or slag phase has higher viscosity, the impact on the refractory lining is expected to be stronger, regardless of a weakened agitation

level. From this point of view, a melt with a higher viscosity would increase the burden on the wall, and is not recommended for industrial applications.

## 5. Conclusions

In this study, the previously used numerical model was further verified. The effect of melt density and viscosity on bath agitation performance in a simulated full-scale SKS copper smelting furnace was

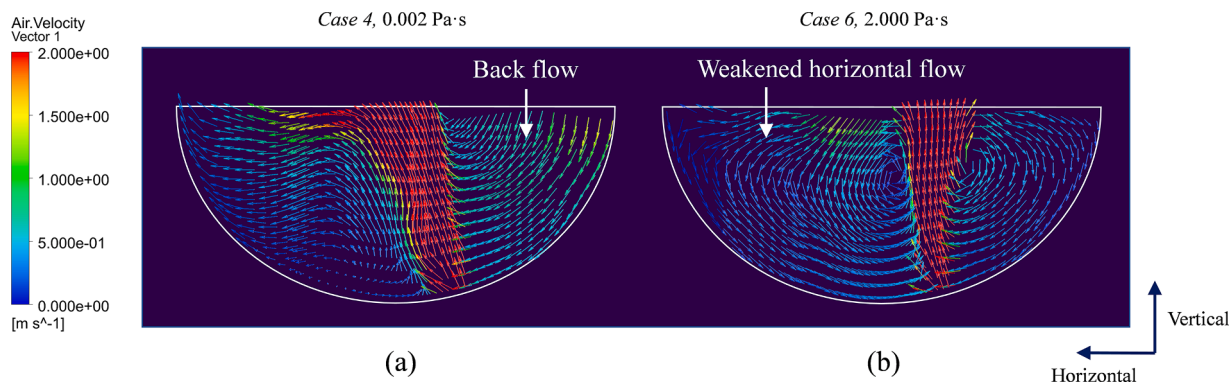


**Fig. 10.** Air velocity vectors in the middle bubble plume sections for Case 4 (a) viscosity 0.002 Pa·s, time 26.25 s and Case 6 (b) 2.000 Pa·s, time 26.25 s. The time is selected at a peak in the volume fraction variation curve (Fig. 4(d)) of the low velocity regions.

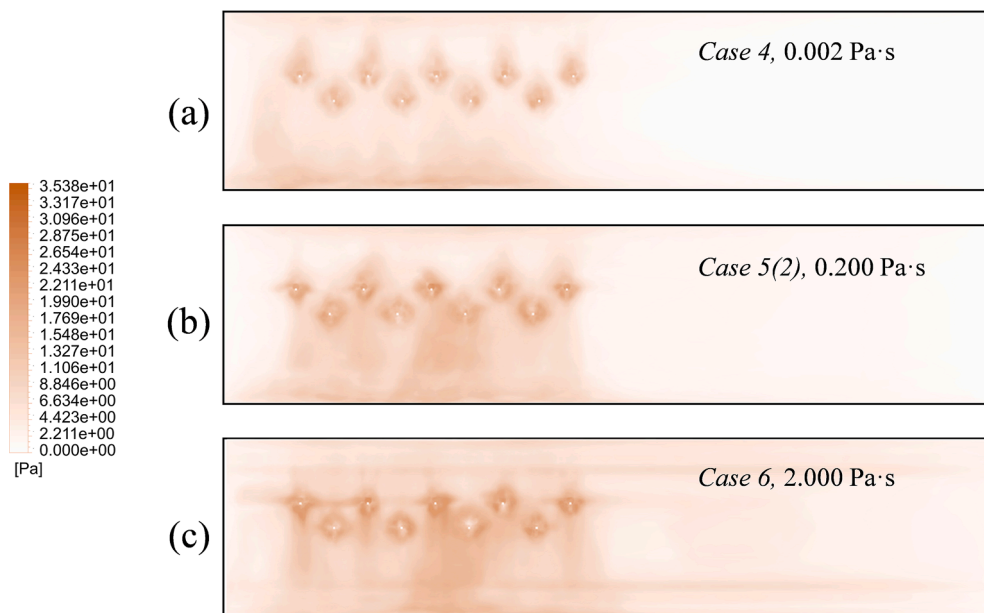


**Fig. 11.** Bottom view of the superimposition of wall shear stress at 20–30 s. The images were taken from each 0.5 s, and each image was set with 95% transparency. Conditions: density:  $4000 \text{ kg/m}^3$ , viscosity: (a) 0.002 Pa·s, (b) 0.200 Pa·s, (c) 2.000 Pa·s.

investigated using the verified model, according to industrial density and viscosity ranges from onsite measurements and reported modeling work. Based on the comparison and analysis of the simulation results, the following conclusions can be drawn:

- 1) The current numerical model was found to be able to accurately calculate a macroscopic multiphase flow in an SKS furnace, in terms of the position of the bubble plume and the standing wave characteristics. The numerical model could be applicable to other bottom blown industrial vessels which have a similar bottom blow tuyeres to that of the SKS furnaces.
- 2) Compared with the tuyere diameter and bath depth, which significantly influence the agitation performance, the density and viscosity in the range applied in industry only slightly affect the agitation, with only a mild change observed in the velocity distribution. Correspondingly, a change of the melt temperature or the melt component which leads to variations of melt density and viscosity in current investigated ranges, is not able to significantly influence the flow field.
- 3) In the studied density and viscosity ranges, a lower melt density or viscosity helps to enhance the flow circulation and back flow, thus

contributing to improved agitation performance and enhanced performance of the furnace.

- 4) In the density and viscosity ranges tested, a lower melt density or viscosity contributes to alleviating the impact on the wall. The melt viscosity has a stronger influence on the wall shear stress. Consequently, lower melt viscosity helps to increase the refractory life span.

#### Declaration of competing interest

No conflict of interest.

#### Data availability

Data will be made available on request.

#### Acknowledgments

The authors are grateful to Fupeng Liu and Yanxin Wu for their density and viscosity measurements at Henan Yuguang Gold Lead Company Limited. This work was supported by the China Scholarship

Council, and the Aalto University School of Chemical Engineering.

### Funding

The research is funded by the China Scholarship Council and Aalto university.

### Supplementary materials

Supplementary material associated with this article can be found, in the online version, at [doi:10.1016/j.ceja.2023.100496](https://doi.org/10.1016/j.ceja.2023.100496).

### References

- [1] Z. Liu, L. Xia, The practice of copper matte converting in China, *Miner. Process. Extr. Metall.* 128 (2019) 117–124.
- [2] B. Zhao, J. Liao, Development of bottom-blowing copper smelting technology: a review, *Metals (Basel)* 12 (2022) 190.
- [3] K. Song, A. Jokilaakso, Transport phenomena in copper bath smelting and converting processes—a review of experimental and modeling studies, *Miner. Process. Extr. Metall.* 43 (2022) 107–121.
- [4] H. Yan, F. Liu, Z. Zhang, Q. Gao, F. Liu, Z. Cui, D. Shen, Influence of lance arrangement on bottom-blowing bath smelting process, *Chin. J. Nonferrous Metals* 22 (2012) 2393.
- [5] Z. Dong, D. Li, X. Yao, L. Min, B. Li, S. Liang, T. Guo, Q. Xue, Research of gas-liquid multiphase flow in oxygen-enriched bottom blown copper melting furnace, *Nonferrous Metal Eq.* 2 (2019) 36–41. In Chinese.
- [6] P. Shao, L. Jiang, Flow and mixing behavior in a new bottom blown copper smelting furnace, *Int. J. Mol. Sci.* 20 (2019) 5757.
- [7] K. Song, A. Jokilaakso, CFD modeling of multiphase flow in an SKS furnace: the effect of tuyere arrangements, *Metal Mater. Trans. B* 52 (2021) 1772–1778.
- [8] K. Song, A. Jokilaakso, CFD modeling of multiphase flow in an SKS Furnace with new tuyere arrangements, *Metal Mater. Trans. B* 53 (2022) 253–272.
- [9] K. Song, A. Jokilaakso, The CFD modeling of multiphase flow in an SKS furnace: the effect of tuyere diameter and bath depth, *JOM* 74 (2022) 1488–1498.
- [10] D.K. Chibwe, G. Akdogan, C. Aldrich, P. Taskinen, Modelling of mixing, mass transfer and phase distribution in a Peirce–Smith converter model, *Can. Metall. Quart.* 52 (2013) 176–189.
- [11] H. Zhao, T. Lu, P. Yin, L. Mu, F. Liu, An experimental and simulated study on gas-liquid flow and mixing behavior in an ISASMELT furnace, *Metals (Basel)* 9 (2019) 565.
- [12] L. Shui, Z. Cui, X. Ma, M.A. Rhamdhani, A. Nguyen, B. Zhao, Mixing phenomena in a bottom blown copper smelter: a water model study, *Metal Mater. Trans. B* 46 (2015) 1218–1225.
- [13] L. Shui, Z. Cui, X. Ma, M.A. Rhamdhani, A. Nguyen, B. Zhao, Understanding of bath surface wave in bottom blown copper smelting furnace, *Metal Mater. Trans. B* 47 (2016) 135–144.
- [14] J. F-Z, D. Sichen, S. Seetharaman, Viscosity measurements on some fayalite slags, *ISIJ Int.* 41 (2001) 722–727.
- [15] E.T. Turkdogan, *Physicochemical Properties of Molten Slags and Glasses*, The Metals Society, London, 1984, pp. 2–27.
- [16] ANSYS Fluent Theory Guide 19.0, 505–510, U.S.A. 2018.
- [17] W. Liu, H. Tang, S. Yang, M. Wang, J. Li, Q. Liu, J. Liu, Numerical simulation of slag eye formation and slag entrapment in a bottom-blown argon-stirred ladle, *Metal Mater. Trans. B* 49 (2018) 2681–2691.
- [18] Z. Zhang, Z. Chen, H. Yan, F. Liu, L. Liu, Z. Cui, D. Shen, Numerical simulation of gas-liquid multi-phase flows in oxygen enriched bottom-blown furnace, *Chin. J. Nonferrous Metals* 22 (2012) 1826–1834. In Chinese.
- [19] F. Liu, Y. Wu, Density and Viscosity Measurements, Henan Yuguang Gold Lead Company Limited. Private communication, 2022.
- [20] D. Wang, Y. Liu, Z. Zhang, T. Zhang, X. Li, PIV measurements on physical models of bottom blown oxygen copper smelting furnace, *Can. Metall. Quart.* 56 (2017) 221–231.
- [21] S. Qu, T. Li, Z. Dong, H. Luan, Discussion on production practice of oxygen-enriched bottom-blown smelting and design improvement of bottom-blown furnace, *Chin. Nonferrous Metal* 1 (2012) 10–13. In Chinese.
- [22] ANSYS Fluent Meshing User's Guide 17.0, 313, U.S.A. 2016.